Analysis of light and no-load operation of a 300 kW resonant single active bridge based on 3.3 kV SiC-devices

Gustavo Fortes, Philippe Ladoux, Joseph Fabre, D. Flumian

▶ **To cite this version:**

Gustavo Fortes, Philippe Ladoux, Joseph Fabre, D. Flumian. Analysis of light and no-load operation of a 300 kW resonant single active bridge based on 3.3 kV SiC-devices. IET Power Electronics, 2022, IET Power Electronics, 15 (14), pp.1540-1549. 10.1049/pel2.12324 . hal-03699138

HAL Id: hal-03699138
https://hal.science/hal-03699138

Submitted on 13 Jun 2023

HAL is a multi-disciplinary open access archive for the deposit and dissemination of scientific research documents, whether they are published or not. The documents may come from teaching and research institutions in France or abroad, or from public or private research centers.

L'archive ouverte pluridisciplinaire **HAL**, est destinée au dépôt et à la diffusion de documents scientifiques de niveau recherche, publiés ou non, émanant des établissements d'enseignement et de recherche français ou étrangers, des laboratoires publics ou privés.

Check for updates

Received: 9 February 2022 | Revised: 31 March 2022 | Accepted: 14 May 2022

IET Power Electronics

DOI: 10.1049/pel2.12324

The Institution of Engineering and Technology WILEY

ORIGINAL RESEARCH

Analysis of light and no-load operation of a 300 kW resonant single active bridge based on 3.3 kV SiC-devices

G. Fortes[1,2] | P. Ladoux[2] | J. Fabre[2,3] | D. Flumian[2]

[1]XPwE Solutions - eXperts in Power Electronics, Belo Horizonte, Brazil

[2]LAPLACE Laboratory, Université de Toulouse, Toulouse, France

[3]SCLE-SFE Company, Toulouse, France

Email: gustavo.fortes@ieee.org

Funding information
H2020 Energy, Grant/Award Number: 881772

Abstract

The resonant single active bridge topology (R-SAB) operated in the half-cycle discontinuous current mode (HC-DCM) is a very attractive solution due to its high efficiency, low complexity and fixed voltage transfer ratio (DCX). However, as expected for a series-resonant converter (SRC), its DCX operation depends on the resonant tank circuit-parameters, parasitic capacitive elements and output load. Specially, at light and no-load operation, when the system is extremely underdamped, it may present a large output over-voltage due to resonance interactions. This is of prime importance for converters using medium voltage (MV) SiC-MOSFETs, which feature significant output capacitances that can lead to voltage breakdown of the rectifier semiconductors. Therefore, the supposed fixed-voltage transfer ratio is not entirely valid and deserves a proper understanding due its criticality. This paper reviews the subject, clarifying its root cause and its multifactorial dependencies. Moreover, it provides a simple solution based on a variable dead-time with fixed magnetizing current experimentally verified with a 300kW/1.8kV R-SAB prototype implemented with MV SiC-devices.

1 | INTRODUCTION

The first DC/DC converter to integrate a transformer and a series-resonant capacitor was introduced in 1970 [1] and, since then, it has been extensively used in many applications [2–4]. In the literature, it can be found also as: series-resonant converter (SRC) [5]; resonant LLC converter [6]; and resonant single active bridge (R-SAB) [7]. It consists of a transformer and a resonant capacitor placed between an active inverter bridge and a diode rectifier bridge, as shown in Figure 1. Its ability to achieve ZCS (zero-current switching), ZVS (zero-voltage switching) and quasi-sinusoidal currents [8] allows it to reach the highest efficiency among other topologies.

It is able to operate in DCX mode [9] which is supposed to provide a fixed-voltage transfer ratio without requiring any closed-loop control [10–12]. However, this is not entirely true under light and no-load operation, since the output voltage increases continuously as the switching frequency increases [13]. This is due to the junction capacitance of the rectifier diodes and the transformers parasitic capacitance causing a high frequency resonant interaction with the transformer leakage inductance.

Some researchers have studied and proposed solutions to overcome such behavior and ensure a wide voltage operation range. Primarily, they can be divided into three categories: (1) the ones that have modified the typical R-SAB circuit adding extra elements for passive damping or active control purposes; (2) the ones that have deployed closed-loop methods, giving up on the DCX principle; (3) the ones that have implemented open-loop methods, in a semi-regulated or unregulated DCX sense [14].

For instance, in the first category, a dummy load resistor is commonly used to ensure reliable operation [13], providing sufficient damping to the system. On the one hand, it prevents the operation under light-load conditions but, on the other hand, it impacts the overall efficiency. Also, an extra LC anti-resonance circuit can be used acting as a band-stop filter [15, 16]. Apart from the extra passive elements and losses, this solution inserts an additional unwanted resonant tank due to its capacitive element and the transformer leakage-inductance, causing higher frequency oscillations over the wide operation range. Other studies have added active elements as, for example, parallel low-power DC-DC converters [17, 18] to control the output voltage, implementing a more complex and costly solution. Another

This is an open access article under the terms of the Creative Commons Attribution-NonCommercial-NoDerivs License, which permits use and distribution in any medium, provided the original work is properly cited, the use is non-commercial and no modifications or adaptations are made.
© 2022 The Authors. *IET Power Electronics* published by John Wiley & Sons Ltd on behalf of The Institution of Engineering and Technology.

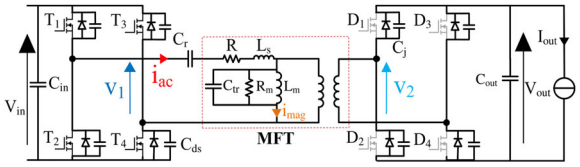

FIGURE 1 Typical resonant single active bridge showing the parasitic elements

control scheme deploys a small phase shift between the primary and secondary bridges of an R-DAB (resonant dual active bridge) converter, supposedly, operated as an R-SAB, when the rectifier is implemented with MOSFETs rather than only diodes [19]. It allows an active sharing of the transformers magnetizing current; however, as this is done by supplying reactive currents from the primary and secondary sides, the total losses are expected to be higher. Besides that, these extra active elements increase the equivalent capacitance and consequently, impact the soft-switching behavior of the converter over the full operation range [20].

Other researchers have suggested a feedback control method for wide range regulation. For instance, very light-load regulation can be achieved by phase-shift [21, 22] or duty-cycle control [23] of the inverter side legs. From the DCX point of view, they increase system complexity with an extra closed-loop control. In addition, as shown in [21], it is only focused on improving the low-load efficiency by means of decreasing the transformer losses, rather than improving the output voltage controllability. Meanwhile, in [22] and [23], they are able to improve light-load regulation using phase-shift and duty-cycle control, which increase their switching losses and consequently, add extra damping to the system. Nevertheless, a hybrid control scheme is also implemented in [23], using an additional frequency modulation (FM) to achieve wide output voltage range. Based on a hysteresis on/off control type, burst mode methods have been also studied [24, 25]. These solutions experience certain voltage and current surges, as expected for an ordinary hysteresis output voltage control.

Finally, in the last category, an optimized fixed dead-time and switching frequency was implemented for wide range operation [26]. However, an idealized model is used to calculate the optimal fixed parameters which does not take into account the junction capacitance of the rectifier diodes and the transformer parasitic capacitance. This leads to some misconceptions such as: to control the output voltage at light or no load, the controller is supposed to increase the switching frequency to the maximum allowable [26], true for an idealized LLC model, as shown in [13]. Another optimal and variable dead-time, with different values for each inverter leg, is proposed in [27]. It provides an inherent burst-mode operation, acting as a hysteresis output voltage control, such as [24, 25], and therefore, suffers from voltage and current surges either. In addition, the analysis does not consider the parasitic capacitance of the transformer and the rectifier. Meanwhile it evaluates a non-resonant PSFB (phase-shift full-bridge) converter operating in CCM (continuous current mode) with phase shift control for wide range operation.

Based on the literature reviewed, it is clear that many methods are implemented for wide operation range and just a few are really focused on the light and no-load operation. Therefore, they tend to use idealized models that are not suitable for the proper understanding of this specific condition, where common assumptions fail, such as: the resonant current is constant during the dead-time; if the leakage inductance is much smaller than the magnetizing inductance of the transformer, it can be ignored; the transformer and the rectifier diodes are ideal devices; voltage and current waveforms can be regarded as sinewaves, ignoring the harmonics; the dead-time between switches can be neglected; inverter mosfets capacitances are negligible.

This article focuses on the analysis of the R-SAB converter at light and no-load operation aiming to sustain its fixed voltage transfer ratio without requiring any closed-loop control (DCX) and avoiding the output overvoltage issue. Specially, this is critical for converters using medium voltage (MV) SiC-MOSFETs, which feature significant output capacitances that could lead to voltage breakdown of the output rectifier devices. This paper revises the assumptions cited before, clarifying the multifactorial dependencies, splitting the issue in the impedance, inverter voltage-source harmonics and theoretical analysis. Moreover, it provides a simple solution based on a variable dead-time with fixed magnetizing current experimentally verified with a 300kW/1.8kV R-SAB prototype implemented with MV SiC-Devices.

2 | LIGHT AND NO-LOAD OPERATION ANALYSIS

2.1 | Characteristic impedance

The harmonic approximation approach is based on the assumption that the fundamental component of the Fourier series of a square-wave voltage has the main contribution to the energy transferred to the output. This relies on the selective nature of resonant tank circuits acting as band pass filters. This approach is able to give accurate results for operating points close to the resonance frequency, while it is less accurate at frequencies below resonance due to discontinuous conduction [28]. Nevertheless, this method is very useful to give an overview of the impedance and the resonant frequencies of the circuit, specially, for light and no-load operation, where the load-dependent effects are negligible.

The proposed equivalent circuit for resonant single active bridge is shown in Figure 2a. As it is focused on the light and no-load operation, elements that are usually not considered, have been taken into account, such as: the transformer winding capacitance (C_{tr}) with a series resistance (R_{tr}) due to the skin effect; the secondary side devices junction capacitances (C_j) and their significant off-resistances (R_j) as their drift regions are unmodulated; the transformer core losses, considered mostly voltage-driven, modelled as a resistance (R_m), and therefore, could provide significant damping effect at light and no-load. The equivalent values shown in Figure 2b are related to the

17554543, 2022, 14, Downloaded from https://ietresearch.onlinelibrary.wiley.com/doi/10.1049/pel2.12324 by Universite De Toulouse 3, Wiley Online Library on [13/06/2023]. See the Terms and Conditions (https://onlinelibrary.wiley.com/terms-and-conditions) on Wiley Online Library for rules of use; OA articles are governed by the applicable Creative Commons License

primary side by the transformer ratio n:

$$R_o = \frac{R_m}{1 + \frac{\pi^2 I_{out}}{8n^2 V_{out}}}, C_e = C_{tr} + \frac{C_j}{n^2}, R_e = \frac{R_{tr} R_j n^2}{R_{tr} + R_j n^2}. \quad (1)$$

The forward transfer function $H(s)$ of the resonant single active bridge can be derived as follows and the final formula is presented in (5), located at the bottom of this page:

$$H_{rsab}(s) = \frac{Z_2(s)}{Z_{in}(s)} = \frac{sL_m || R_e + \frac{1}{sC_e} || R_o}{\frac{1}{sC_r} + sL_m + Z_2}. \quad (2)$$

The DC conversion ratio (M) can be derived using (3) followed by reformulation based on the terms defined in (4) which are: normalized frequency (f_n); resonant frequency (ω_0); quality factor (Q); and three different impedance factors (K_0, K_1, K_2). The final formula is presented in (6) located at the bottom of this page.

$$M = ||H_{rsab}(s)||_{s=j\omega_s}, \quad (3)$$

$$f_n = \frac{\omega_s}{\omega_0}, \omega_0 = \frac{1}{\sqrt{L_s C_r}}, Q = \frac{1}{R_o}\sqrt{\frac{L_s}{C_r}},$$
$$K_0 = \frac{L_m}{L_r}, K_1 = \frac{C_e}{C_r}, K_2 = \frac{R_e}{R_o}. \quad (4)$$

2.2 | Inverter voltage source harmonic spectrum

The inverter-side voltage (V_1) is the source of the harmonic spectrum that supplies the resonant circuit. Figure 3 shows simplified scenarios (1, 2 and 3) for the inverter voltage profile during a soft switching event in DCM mode. It is dependent on the magnetizing current (i_{mag}), dead-time (t_{dead}) and the equivalent capacitance (C_{eq}). Specially, in Scenario 1, it shows an incomplete ZVS switching that is most likely to happen with a significant equivalent capacitance, such as those present in MV SiC-MOSFETs.

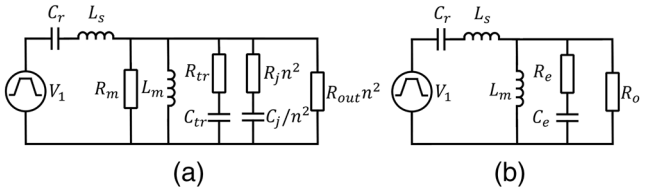

FIGURE 2 (a) Proposed R-SAB equivalent circuit for computing the harmonic approximation focused at light and no-load operation. (b) Simplified equivalent values

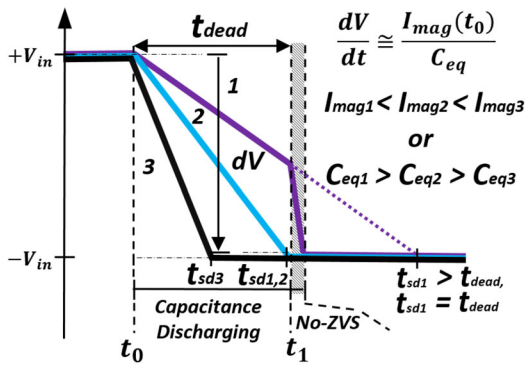

FIGURE 3 Three simplified scenarios of the inverter voltage profile during a soft switching event in DCM mode at light and no-load operation

After all, these scenarios mean different harmonic spectra that can be expressed using Fourier series (Equation 7):

$$V_1(t) = \frac{4V_{in}}{\pi} \sum_{n=1,3,5}^{\infty} \frac{1}{h} \left(\frac{I_{mag}(t_0) t_{sd}}{2C_{eq} V_{in}} \left(\frac{1}{h} \frac{2}{\omega_s t_{dead}} \right. \right.$$
$$\left. \left. sin\left(\frac{h\omega_s t_{sd}}{2} \right) - 1 \right) + 1 \right) sin(n\omega_s t), \quad (7)$$

where $I_{mag}(t_0)$ is the magnetizing current at t_0, $C_{eq} = (C_{ds} + C_{tr} + C_j/n^2)$ is the equivalent capacitance during the period and t_{sd} is the soft discharge-time where, if $t_{sd} > t_{dead}$, $t_{sd} = t_{dead}$.

Figure 4 shows the three-dimensional inverter voltage-gain curve (Equation 6) for light and no-load operation alongside

$$H(s) = \frac{s^3 L_m R_e C_e C_r + s^2 L_m C_r}{s^4 L_s L_m \left(\frac{R_e}{R_o} + 1\right) C_r C_e + s^3 L_s C_r \left(\frac{L_m}{R_o} + R_e C_e \left(1 + \frac{L_m}{L_s}\right)\right) + s^2 \left(L_m C_e \left(\frac{R_e}{R_o} + 1\right) + C_r (L_m + L_s)\right) + s \left(\frac{L_m}{R_o} + R_e C_e\right) + 1} \quad (5)$$

$$M(f_n) = \sqrt{\frac{(f_n^2 K_0)^2 + \left(f_n^3 \frac{1}{Q} \frac{K_0}{\omega_0} \frac{K_1}{K_2}\right)^2)}{(f_n^2 K_0 K_1 (K_2 + 1)(f_n^2 - 1) - f_n^2 (1 + K_0) + 1)^2 + \left(f_n Q (1 - f_n^2) + f_n \frac{1}{Q} K_1 K_2 \left(1 - f_n^2 - \frac{f_n^2}{K_0}\right)\right)^2}} \quad (6)$$

17554543, 2022, 14, Downloaded from https://ietresearch.onlinelibrary.wiley.com/doi/10.1049/pel2.12324 by Universite De Toulouse 3, Wiley Online Library on [13/06/2023]. See the Terms and Conditions (https://onlinelibrary.wiley.com/terms-and-conditions) on Wiley Online Library for rules of use; OA articles are governed by the applicable Creative Commons License

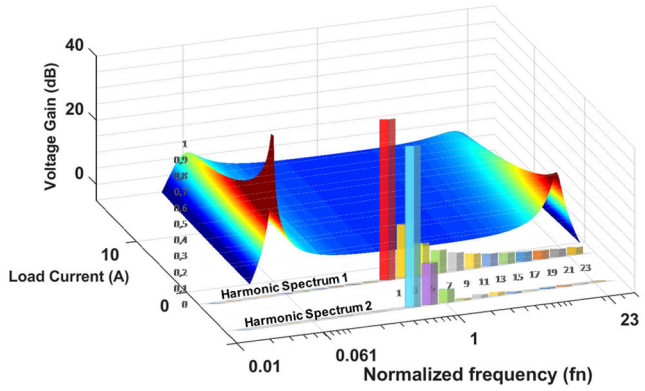

FIGURE 4 Three-dimensional gain curve for light and no-load operation besides an expected inverter voltage harmonics source

TABLE 1 Simulation parameters based in the experimental value

Parameters	Values	Units
Transformer total leakage inductance	$L_s = 22.5$	μ H
Transformer magnetizing inductance	$L_{mag} = 5.7$	*mH*
Transformer winding capacitance	$C_{tr} = 2.0$	*nF*
Series transf. skin-effect resistance	$R_{tr} = 1.0$	Ω
Transformer core losses resistance	$R_m = 8350$	Ω
Transformer ratio	$n = 1.0$	
Series resonance capacitor	$C_r = 3.0$	μ F
Junction capacitance (FMF750DC)	$C_j = 6.0$	*nF*
Junction off-resistance (FMF750DC)	$R_j = 10.0$	Ω
Inverter switching dead time	$t_{dead} = 5.0$	μ s

the expected harmonic spectra (Equation 7) regarding Scenarios 1 and 2. The resonant simulation parameter-values used are based on the experimental ones presented in Table 1, where the same FMF750DC devices are considered at the inverter and rectifier sides. In addition, Matlab and PLECs have been used for implementing the derived equations.

Hence, from a macro point of view, an argument for the overvoltage issue lies in the interactions between the harmonic spectra and the characteristic impedance of the resonant single active bridge. At light and no-load operation, the converter is not damped enough, revealing its multi-resonant behavior. In these conditions, it loses its selective frequency nature providing a pass for a broader range of frequencies. This is critical at higher frequencies due to the resonance caused by the equivalent capacitance and the resonant inductance (L_s), as previously discussed. At this point, the harmonic spectrum of the inverter voltage-source is responsible for exciting this resonance. The amount of higher order harmonics from the source has a multi-factorial dependency related to the inverter voltage-source profile (Equation 7). For instance, it becomes clear when comparing the harmonic spectra from Scenarios 1 and 2 shown in Figure 4, as the amount of higher frequency harmonics are significantly lower for the second case, avoiding the over excitation of the high frequency resonance.

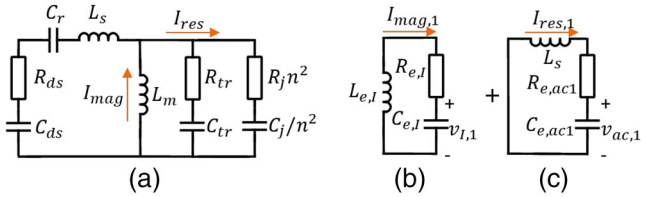

FIGURE 5 Time interval 1: (a) Simplified equivalent circuit divided into its (b) low and (c) high frequency parts

2.3 | Time domain analysis

Due to its multi-resonance nature an exact form analysis can be used to determine individual equations and describe, more accurately, each converter operating sequence. Hence, the circuit should be evaluated at different time scales during each time interval, with regards to its distinct resonance frequencies and equivalent impedances. In order to model and understand the overvoltage issue from this micro-perspective, the same subsequent intervals, shown in Figure 3, have been analyzed as follows:

Time interval 1 ($t_0 < t < t_1$): This is the dead-time period, when all primary and secondary devices are OFF. Their output capacitances are charged/discharged by means of the magnetizing current circulating in the transformer. It flows in opposite directions between the primary and secondary, dividing as a function of the capacitive divider formed. The worst case for the overvoltage issue is at no-load operation ($R_o >> R_e$). At this point, the equivalent circuit shown in Figure 2 can be simplified as shown in Figure 5a and separated into its low (b) and high (c) frequency parts.

Hence, the following equations can be derived from the equivalent circuits:

$$v_{I,1}(t) = \frac{e^{-\alpha_I t}}{\omega_{d,I}}\left(\omega_{d,I} V_I(t_0) cos(\omega_{d,I} t) + \left(\frac{I_{mag}(t_0)}{C_{e,I}} + \alpha_I V_I(t_0)\right) sin(\omega_{d,I} t)\right), \quad (8)$$

$$v_{ac,1}(t) = \frac{e^{-\alpha_{ac,1} t}}{\omega_{d,ac1}}\left(\frac{I_{res,1}(t_0)}{C_{e,ac1}} sin(\omega_{d,ac1} t)\right), \quad (9)$$

$$I_{mag,1}(t) = \frac{I_{mag}(t_0) e^{-\alpha_I t}}{\omega_{d,I}}\left(\omega_{d,I} cos(\omega_{d,I} t) + \left(\alpha_I - \frac{R_{e,I}}{L_{e,I}} + \frac{V_I(t_0)}{I_{mag}(t_0) L_{e,I}}\right) sin(\omega_{d,I} t)\right), \quad (10)$$

$$I_{res,1}(t) = \frac{I_{res,1}(t_0) e^{-\alpha_{ac,1} t}}{\omega_{d,ac1}}\left(\omega_{d,ac1} cos(\omega_{d,ac1} t) + \left(\alpha_{ac,1} - \frac{R_{e,ac1}}{L_s} -\right) sin(\omega_{d,ac1})\right), \quad (11)$$

17554543, 2022, 14, Downloaded from https://ietresearch.onlinelibrary.wiley.com/doi/10.1049/pel2.12324 by Universite De Toulouse 3, Wiley Online Library on [13/06/2023]. See the Terms and Conditions (https://onlinelibrary.wiley.com/terms-and-conditions) on Wiley Online Library for rules of use; OA articles are governed by the applicable Creative Commons License

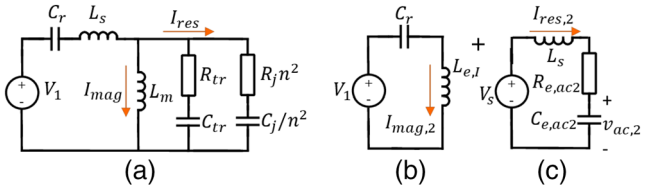

FIGURE 6 Time interval 2: (a) Simplified equivalent circuit divided into its (b) low and (c) high frequency parts

where α is the damping factor, ω_d is the damped frequency. The indexed values for each part are as follows:

$$R_{e,I} = \frac{R_{ds}R_{tr}R_j n^2}{R_{ds}R_{tr} + R_{tr}R_j n^2 + R_{ds}R_j n^2}, L_{e,I} = L_m + L_s,$$

$$C_{e,I} = \frac{C_{ds}C_r}{C_{ds}+C_r} + C_{tr} + \frac{C_j}{n^2}, R_{e,ac1} = R_{ds} + \frac{R_{tr}R_j n^2}{R_{tr}+R_j n^2},$$

$$C_{e,ac1} = \frac{C_{ds}C_r(C_{tr}+C_j/n^2))}{(C_{ds}C_r + (C_{ds}+C_r)(C_{tr}+C_j/n^2)},$$

$$\omega_{d,I} = \sqrt{\frac{1}{(L_{e,I}C_{e,I}} - \alpha_I^2}, \alpha_I = \frac{R_{e,I}}{2L_{e,I}},$$

$$\omega_{d,ac1} = \sqrt{\frac{1}{L_s C_{e,ac1}} - \alpha_{ac,1}^2}, \alpha_{ac,1} = \frac{R_{e,ac1}}{2L_s}, \quad (12)$$

and the initial conditions are:

$$I_{res,1}(t_0) = I_{mag}(t_0)\frac{C_{tr}+C_j/n^2}{C_{e,I}}, V_I(t_0) = -V_{in}. \quad (13)$$

This interval is commonly modelled as a simple integration with a constant magnetizing current. Nevertheless, in some cases, this assumption fails to define proper initial conditions to the next interval. It is important to model it using the exact form in several cases, such as: for light and no-load conditions where the high frequency part is more significant; when the soft-discharge time (t_{sd}) lengthens and approaches the low-frequency period ($1/w_{d,I}$), hence, the constant magnetizing-current assumption becomes invalid; or the soft-discharge time (t_{sd}) shortens and approaches the high-frequency period ($1/w_{d,ac1}$), increasing its influence in the next interval.

Time interval 2 ($t_1 < t < t_2$): During this period, the inverter devices are turned-on, meanwhile the rectifier diodes can be in the ON or OFF-states, depending on the load conditions. At steady-state, no-load and assuming $R_o >> R_e$, the rectifier diodes are in the off-state and the equivalent circuit is shown in Figure 6a. At this condition, the voltage peak across the diodes corresponds to the maximum converter output voltage.

Hence, the following response equations can be derived from the decoupled equivalent circuits, shown in Figure 6b,c:

$$v_{ac,2}(t) = \frac{e^{-\alpha_{ac,2}t}}{\omega_{d,ac2}}\left(\omega_{d,C2}V_{ac2}(t_1)cos(\omega_{d,ac2}t) + \left(\frac{I_{res,2}(t_1)}{C_{e,ac2}} + \alpha_{ac,2}V_{ac,2}(t_1)\right)sin(\omega_{d,ac2}t)\right), \quad (14)$$

$$I_{res,2}(t) = \frac{I_{res,2}(t_1)e^{-\alpha_{ac,2}t}}{\omega_{d,ac2}}\left(\omega_{d,ac2}cos(\omega_{d,ac2}t) + \left(\alpha_{ac,2} - \frac{R_{e,ac2}}{L_s} -\right)sin(\omega_{d,ac2})\right), \quad (15)$$

$$I_{mag,2}(t) = I_{mag}(t_1)cos(\omega_{0,I}t) + \frac{V_I(t_0)}{L_{e,I}}\Big)sin(\omega_{0,I}t), \quad (16)$$

where the indexed values for each part are as follows:

$$R_{e,ac2} = R_{tr} + R_j n^2, L_{e,I} = L_m + L_s,$$

$$C_{e,ac2} = \frac{C_r(C_{tr}+\frac{C_j}{n^2})}{C_r + C_{tr} + \frac{C_j}{n^2}}, \omega_{0,I} = \sqrt{\frac{1}{(L_{e,I}C_r}},$$

$$\omega_{d,ac2} = \sqrt{\frac{1}{L_s C_{e,ac2}} - \alpha_{ac,2}^2}, \alpha_{ac,2} = \frac{R_{e,ac2}}{2L_s}, \quad (17)$$

and the initial conditions are:

$$I_{res,2}(t_1) = I_{res,1}(t_1) + I_{mag,1}(t_1)\frac{C_{tr}+C_j/n^2}{C_{e,I}},$$

$$V_{ac,2}(t_{t1}) = V_{ac,1}(t_1)\frac{C_{e,ac1}}{C_{e,ac2}} - V_s, V_s = -V_1 - v_{I,1}(t_1). \quad (18)$$

As expected, the high-frequency resonance interaction between Time Intervals 1 and 2 plays an important role in defining the initial conditions of Interval 2: $I_{res,2}(t_1)$ and $V_{ac,2}(t_1)$. Both initial conditions are resonant in nature leading to an output voltage that is also dependent on the specific time (t_1). As predicted by Equation (13), the initial conditions define the amplitude of the natural response oscillation. For instance, if time instant t_1 occurs when initial condition $V_{ac,1}(t_1)$ is crossing zero voltage, the overvoltage would be reduced. This could be a useful tool for avoiding the overvoltage issue, when t_1 is precisely designed. Nonetheless, it would not be a simple task because it is supposed to be done at high frequencies, well above the operating converter resonant frequency. In this regard, the initial conditions, originating from the high-frequency part, also decrease exponentially due to the damping factor (α_{ac}). Therefore, they become less important whether the soft-discharge time (t_{sd}) is longer or the magnetizing current is lower. At the limit, only the initial condition from the low-frequency part would be effective, once the high frequency oscillation has been completely damped. Here, a major difference between low

17554543, 2022, 14, Downloaded from https://ietresearch.onlinelibrary.wiley.com/doi/10.1049/pel2.12324 by Universite De Toulouse 3, Wiley Online Library on [13/06/2023]. See the Terms and Conditions (https://onlinelibrary.wiley.com/terms-and-conditions) on Wiley Online Library for rules of use; OA articles are governed by the applicable Creative Commons License

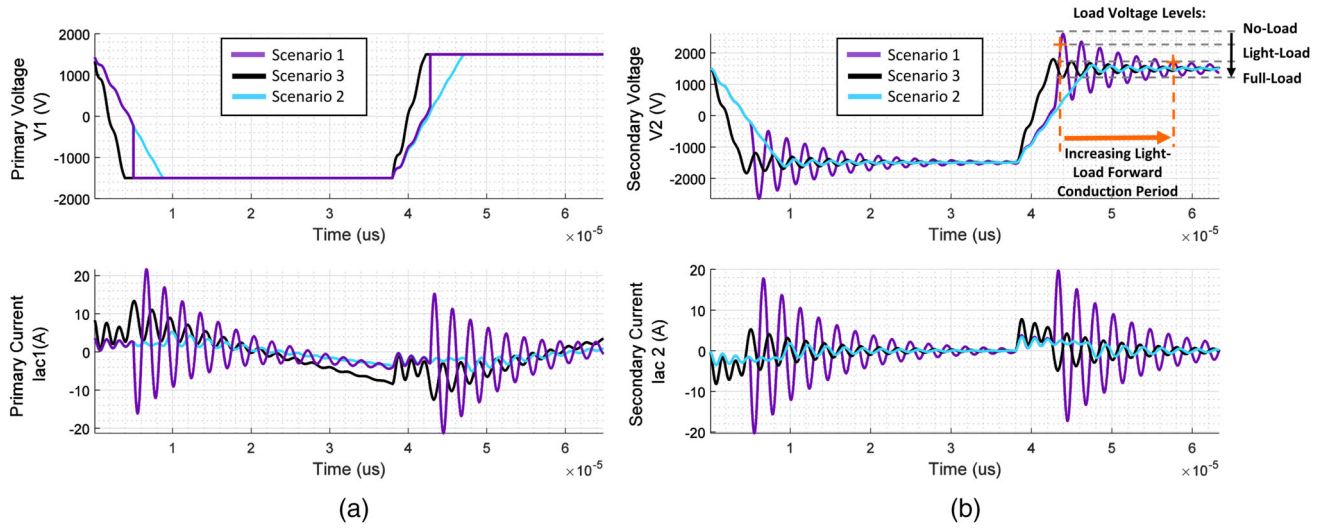

FIGURE 7 Calculated voltage and current from (a) primary and secondary (b) for the no-load and steady state operation under Scenarios 1, 2 and 3.

and high-power converter designs appears. On the one hand, the low power converters tend to have very high switching-frequency, low equivalent capacitance and very fast discharge times. On the other hand, high power converters usually have lower switching frequency, higher equivalent capacitance and lower discharge times. Hence, the low power converter would be more sensitive to the high-frequency-part initial condition ($V_{ac,1}(t_1)$) and it becomes even more significant as the discharge time approximates to the high-frequency resonance period ($1/\omega_{d,ac1}$).

Furthermore, it is essential to note that, when ZVS switching is not perfectly achieved (Scenario 1 - the initial condition $V_{I,1}(t_1)$ does not reach V_1, a voltage step response ($V_s = V_1 - V_{I,1}(t_1) \approx 0$) is obtained from the resonant circuit, causing larger voltage oscillations across the secondary devices.

The obtained equations have been evaluated and the results are presented in Figure 7a, regarding the scenarios shown in Figure 3, with the following differences: Scenario 3 corresponds to the higher value of magnetizing current and Scenario 2 corresponds to the larger dead-time. Analyzing the secondary-side results from Figure 7b, it is fair to say that decreasing the voltage slew rate would result in lower overvoltage up to the limit of lost ZVS operation.

In addition, Figure 7b shows the load voltage levels expected for different loads. For example, when the output voltage is below the no-load voltage level, the secondary diodes would be forward biased until the output capacitance voltage exceeds the device's voltage. Hence, the converter would be operating in a third mode (diodes forward conduction) during the period necessary to transfer energy to the load. Usually, depending on the amount of energy requested for light load, the energy stored in the resonant inductance (L_s) can be sufficient and would be supplied through the high-frequency oscillations. Practically, it results in a light-load conduction period that increases continuously till it reaches the limit for full conduction, as represented in Figure 7b. At this stage, the output voltage will be lower than the input voltage and the behavior of the resonant converter corresponds to an internal voltage-drop proportional to the output current.

TABLE 2 RSAB prototype specifications

Parameters	Values	Units
Input voltage	$V_{in} = 1800$	V
Output voltage	$V_{out} = 1800$	V
Nominal output current	$I_{out} = 170$	A
Nominal output power	$P_{out} \approx 300$	kW
Switching frequency	$f_{sw} = 15.0$	kHz
Inverter switching dead time	$t_{dead} = 5.0$	μ s
SiC-MOSFET - FMF750DC	$C_{ds} = 6.0$	nF
SiC-MOSFET - FMF375DC	$C_{ds} = 3.0$	nF
Full SiC-Diode - FD750DC	$C_j = 1.0$	nF
DC Link capacitor	$C_{in/out} = 60.0$	μ F
Resonance frequency	$f_0 = 19.37$	kHz

3 | VARIABLE DEAD-TIME WITH FIXED MAGNETIZING CURRENT

A variable dead-time with fixed magnetizing current has been implemented in order to avoid a possible voltage breakdown of the rectifier semiconductors at no-load operation. Further, it allows maintenance of the fixed voltage ratio mode (DCX) without requiring any closed-loop control.

This method is suitable for the case corresponding to Scenario 1. It consists of increasing the dead time at light-load operation, in order to increase gradually the soft-switching time. At the limit of no-load operation, as represented by the dashed line in Figure 3, the switching time would be long enough ($t_{sd} = t_{dead}$ and $V_s = 0$) to avoid the larger voltage-step response from the resonant circuit. However, the magnetizing current

17554543, 2022, 14, Downloaded from https://ietresearch.onlinelibrary.wiley.com/doi/10.1049/pel2.12324 by Universite De Toulouse 3, Wiley Online Library on [13/06/2023]. See the Terms and Conditions (https://onlinelibrary.wiley.com/terms-and-conditions) on Wiley Online Library for rules of use; OA articles are governed by the applicable Creative Commons License

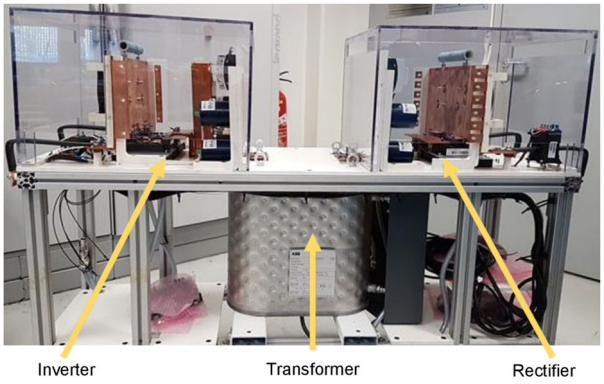

FIGURE 8 Resonant single active bridge test bench rated to 1.8 kV and 170 A

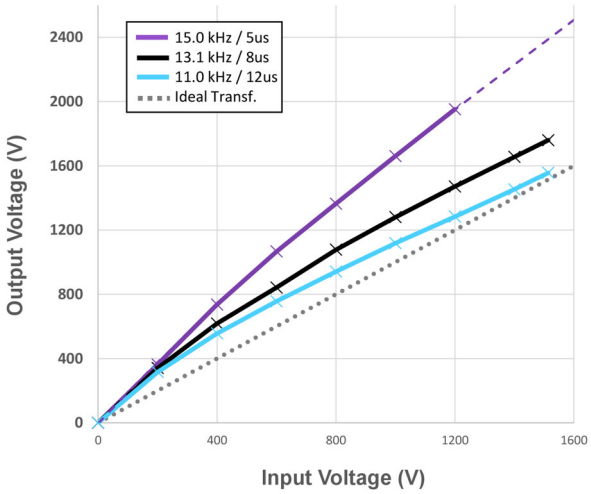

FIGURE 9 Experimental results: Voltage transfer ratio of the converter using FMF750DC devices under no-load operation with different dead-times

is inversely proportional to the dead-time, which is the most important initial condition:

$$I_{mag}(t_0) = \frac{V_{in}(1 - 2t_{dead}\, f_{sw})}{L_{e,I}\, f_{sw}}. \tag{19}$$

Therefore, it is necessary to maintain the magnetizing current constant to get a linear voltage variation. This is achieved by decreasing the switching frequency (f_{sw}) as a function of the dead-time variation:

$$f_{sw} = \frac{V_{in}}{L_{e,I} I_{mag}(t_0) + 2t_{dead}}. \tag{20}$$

Finally, over the complete operating range of the converter, the dead-time should respect the following equation:

$$t_{dead}(i_o) = \begin{cases} \dfrac{t_{dead\_Full}}{V_{in} - V_s/2}\left(V_{in} - \dfrac{V_s/2}{I_{o\_min}} i_o\right), & 0 \le i_o \le I_{o\_min} \\ t_{dead\_Full}, & i_o \ge I_{o\_min} \end{cases}, \tag{21}$$

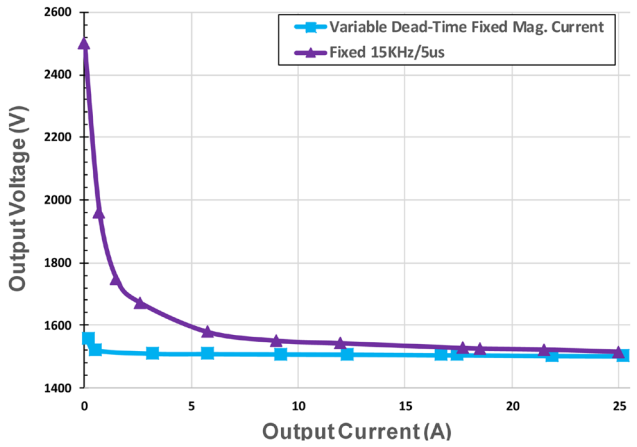

FIGURE 10 Experimental results: Comparison of the R-SAB output characteristics at light and no-load operation with fixed designed dead-time and with the variable dead-time with fixed magnetizing current operation ($V_{in} = 1500V$ and FMF750DC devices)

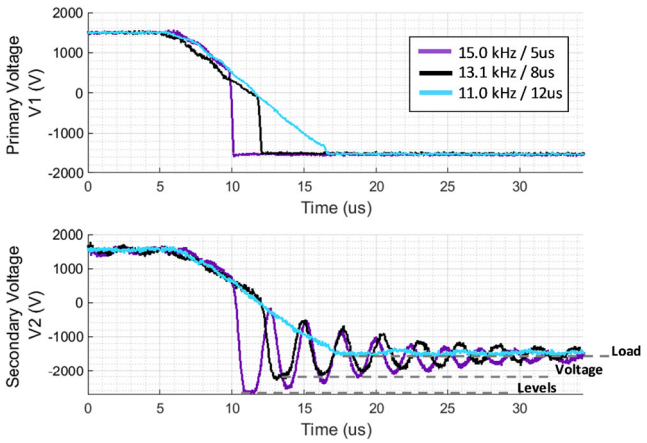

FIGURE 11 Experimental waveforms of the primary and secondary voltages, (V_1 and V_2) using FMF750DC devices at steady-state and no-load operation

where i_o is the output current, I_{o_min} is the output current value below which the output voltage becomes greater than the input voltage and t_{dead_Full} is the dead time usually optimized for full-load operation.

As the dead-time and the switching frequency are supposed to change dynamically in respect to the output current, it is important to set a requirement that ensure a proper controllability in terms of limiting the time response of the output current variation. Therefore, it should be between 5 and 10 times slower than the switching frequency period. For instance, it is quite reasonable for high power railway applications where the time response of the demanded output current is couple of seconds, due to very large line inductance. In other hand, in case of one application where the output current dynamic is much faster, for instance, the switching frequency and dead-time could jump straight to the no-load values defined by Equations (20) and (21).

17554543, 2022, 14, Downloaded from https://ietresearch.onlinelibrary.wiley.com/doi/10.1049/pel2.12324 by Universite De Toulouse 3, Wiley Online Library on [13/06/2023]. See the Terms and Conditions (https://onlinelibrary.wiley.com/terms-and-conditions) on Wiley Online Library for rules of use; OA articles are governed by the applicable Creative Commons License

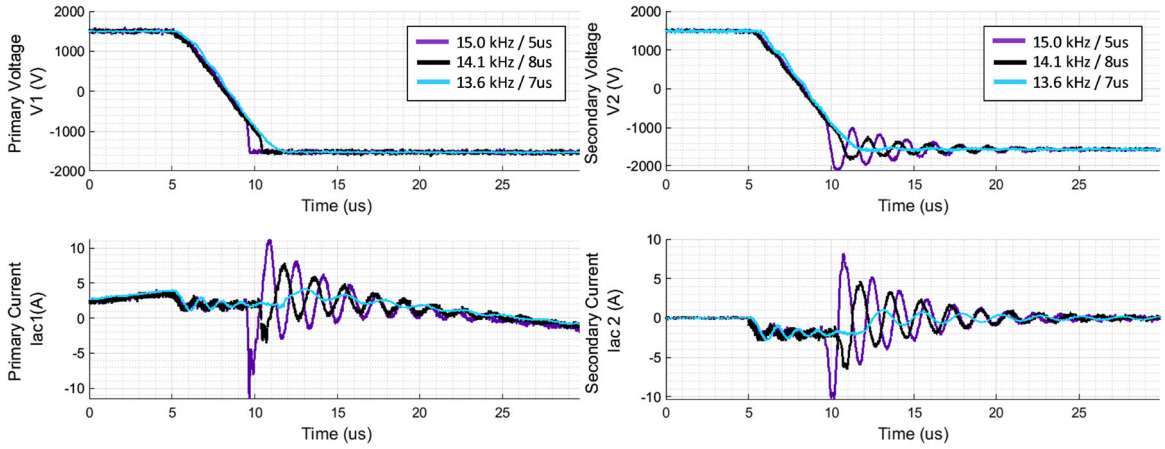

FIGURE 12 Experimental waveforms of the (a) primary and (b) secondary voltages/currents) using devices with lower output capacitances at steady-state and no-load operation (FMF375DC MOSFETS at the inverter and FD750DC Full SiC-Diodes at the rectifier)

4 | RESULTS

Table 2 presents general specifications of the R-SAB prototype (Figure 8) for rated values and its semiconductor devices. For the main parameters of the medium frequency transformer and the resonant circuit, please refer to Table 1. A water-cooled 300 kW prototype rated to 1.8 kV and 170 A was used [29] to obtain the experimental results. It is based on the following major parts: ABBs water-cooled medium-frequency oil-immersed transformer; Mersen's water cooled heatsinks; HC5 series-resonant capacitors from Illinois; LH3 series DC-link capacitors from Electronic Concept; LEMs series LV and DV sensors; Imperixs BoomBox control with optical interfaces; customized gate-drivers [30]; Mitsubishi HBM 3.3 kV SiC-MOSFETs. Specially, the SiC-MOSFET devices used have encapsulated anti-parallel SiC-Diodes, therefore the intrinsic body diode of the MOSFETs are not a concern in this case. Otherwise, it could lead to higher conduction losses during dead-time period.

Figure 9 shows the voltage ratio of the converter with FMF750DC devices at the inverter and rectifier sides. As expected, at no-load condition with the designed $5\mu s$ dead-time [29], the voltage ratio exceeds the transformers unity turns ratio. The output voltage could overcome the breakdown voltage of the rectifier devices. However, modifying the dead-time to $8\mu s$ and $12\mu s$, while keeping the initial magnetizing current constant using Equation (19) to modify the switching frequency, it is clear that the behavior of the converter approximates (at rated input voltage) to the one expected for an ideal transformer.

Figure 10 shows the light and no-load output characteristics of the R-SAB for the designed fixed dead-time and for the new variable dead-time with fixed magnetizing current operation. Thus, the overvoltage issue is solved, while the converter is able to operate in DCX mode providing a fixed voltage ratio without requiring any closed-loop control, extra passive elements or semiconductor devices.

Figure 11 shows the voltage waveforms at the primary and secondary sides, (V_1 and V_2) for the same scenarios, as shown in Figure 9. As expected, these experimental results confirm the improvement of inverter voltage waveforms during the commutations, avoiding the voltage step-response of the high-frequency resonance-circuit, as shown in Figure 6c. This means lower voltage peaks across the rectifier diodes and, consequently, a lower converter output voltage, as predicted by the mathematical analysis presented.

A typical way of improving the switching behavior of the converter and ultimately, its operation at light and no-load is to design the transformer with a higher magnetizing current. However, this leads to additional conduction losses and as shown by [31], to some additional commutations at the secondary side, also increasing the overall losses. Therefore, it would be reasonable to design a transformer with low magnetizing current, nonetheless, the choice of devices with lower output capacitances would be necessary to reach perfect ZVS. In this regard, even though using MV high power SiC-MOSFETS in the rectifier (higher output capacitance), the proposed solution successfully allowed operation at no-load, despite the use of a transformer with low magnetizing current. In addition, to evaluate the influence of lower equivalent capacitance, a new set of devices was used: FMF375DC MOSFETS replaced the inverter devices and Full SiC-Diode modules (FD750DC) replaced the rectifier devices (Table 2). As can be seen from Figure 12, the overvoltage at the secondary side decreased with respect to the dead-time necessary to reach perfect ZVS switching, due to less equivalent capacitance. As expected, the magnetizing current initial condition ($t_1 = 5\mu s$) remained constant among the scenarios, providing a linear soft-switching behavior. Finally, it is important to notice that the results show a particularly good correlation to the theoretical waveform analysis.

5 | CONCLUSION

This paper has analyzed a Full-SiC Resonant Single Active Bridge converter at light and no-load operation under two different forms: first, modeling the converter using harmonic

17554543, 2022, 14, Downloaded from https://ietresearch.onlinelibrary.wiley.com/doi/10.1049/pel2.12324 by Universite De Toulouse 3, Wiley Online Library on [13/06/2023]. See the Terms and Conditions (https://onlinelibrary.wiley.com/terms-and-conditions) on Wiley Online Library for rules of use; OA articles are governed by the applicable Creative Commons License

approximation, while taking into account some parasitic elements usually neglected but very important at light and no-load operation. Second, due to its multi-resonance nature, a theoretical analysis was used to determine the expressions of current and voltage waveforms to describe more precisely the converter intervals. This detailed analysis has clarified the multifactorial dependencies related to the parasitic elements, inverter voltage harmonic spectrum and to the resonant initial conditions among converter modes, in a more mathematical form. Specially, for converters using medium voltage (MV) SiC-devices, which feature significant output capacitances, the overvoltage issue has been considered and experimentally verified with a 300kW/1.8kV R-SAB prototype implemented with a different set of devices. Finally, a variable dead-time with fixed magnetizing current scheme has been implemented to avoid the no-load operation issue and, further, to provide a fixed voltage transfer ratio without requiring any closed-loop control, extra passive elements or semiconductor devices.

ACKNOWLEDGEMENTS

This work is supported by the Future Unied DC Railway Electrication System project FUNDRES (Shift2Rail, Nř 881772) funded by H2020.

CONFLICT OF INTEREST

The authors have declared no conflict of interest.

DATA AVAILABILITY STATEMENT

The data that support the findings of this study are available from the corresponding author upon reasonable request.

ORCID

G. Fortes https://orcid.org/0000-0002-4032-9180
P. Ladoux https://orcid.org/0000-0002-2697-8707
J. Fabre https://orcid.org/0000-0002-1010-3404

REFERENCES

1. Schwarz, F.: A method of resonant current pulse modulation for power converters. IEEE Trans. Ind. Electron. Control Instrum. IECI-17(3), 209–221 (1970)
2. Fu, D., Lu, B., Lee, F.: 1 MHz high efficiency LLC resonant converters with synchronous rectifier. In: IEEE Power Electronics Specialists Conference, pp. 2404–2410. IEEE, Piscataway (2007)
3. Musavi, F., Craciun, M., Gautam, D., Eberle, W., Dunford, W.: An LLC resonant DC-DC converter for wide output voltage range battery charging applications. IEEE Trans. Power Electron. 28(12), 5437–5445 (2013)
4. Fu, D., Liu, Y., Lee, F., Xu, M.: A novel driving scheme for synchronous rectifiers in LLC resonant converters. IEEE Trans. Power Electron. 24(5), 1321–1329 (2009)
5. Vorperian, V., Cuk, S.: A complete DC analysis of the series resonant converter. In: IEEE Power Electronics Specialists conference, pp. 85–100. IEEE, Piscataway (1982)
6. Gu, Y., Lu, Z., Hang, L., Qian, Z., Huang, G.: Three-level LLC series resonant DC/DC converter. IEEE Trans. Power Electron. 20(4), 781–789 (2005)
7. Stackler, C., et al.: NPC assessment in insulated DC/DC converter topologies using SiC MOSFETs for power electronic traction transformer. In: 20th International Symposium on Power Electronics (Ee), pp. 1–6. IEEE, Piscataway (2019)
8. Rothmund, D., Huber, J., Kolar, J.: Operating behavior and design of the half-cycle discontinuous-conduction-mode series-resonant-converter with small DC link capacitors. In: IEEE 14th Workshop on Control and Modeling for Power Electronics (COMPEL), pp. 1–9. IEEE, Piscataway (2013)
9. Dou, S., Wu, W., Pratt, A., Kumar, P.: DC Transformer with line frequency ripple cancellation. In: CES/IEEE 5th International Power Electronics and Motion Control Conference, pp. 1–5. IEEE, Piscataway (2006)
10. Yang, B., Lee, F., Zhang, A., Huang, G.: LLC resonant converter for front end DC/DC conversion. In: APEC. Seventeenth Annual IEEE Applied Power Electronics Conference and Exposition, vol. 2, pp. 1108-1112. IEEE, Piscataway (2002)
11. Huber, J., Ortiz, G., Krismer, F., Widmer, N., Kolar, J.: - Pareto optimization of bidirectional half-cycle discontinuous-conduction-mode series-resonant DC/DC converter with fixed voltage transfer ratio. In: Twenty-Eighth Annual IEEE Applied Power Electronics Conference and Exposition (APEC), pp. 1413–1420. IEEE, Piscataway (2013)
12. Dujic, D., et al., Power electronic traction transformer-low voltage prototype. IEEE Trans. Power Electron. 28(12), 5522–5534 (2013)
13. Lee, B., Kim, M., Kim, C., Park, K., Moon, G.: Analysis of LLC resonant converter considering effects of parasitic components. INTELEC 2009-31st International Telecommunications Energy Conference, pp. 1–6. IEEE, New York (2009)
14. Feng, W., Mattavelli, P., Lee, F.: Pulsewidth locked loop (PWLL) for automatic resonant frequency tracking in LLC DC–DC transformer (LLC-DCX). IEEE Trans. Power Electron. 28(4), 1862–1869 (2013)
15. Yeon, C., Kim, J., Park, M., Lee, I., Moon, G.: Improving the light-load regulation capability of LLC series resonant converter using impedance analysis. IEEE Trans. Power Electron. 32(9), 7056–7067 (2017)
16. Jin, X., Hu, H., Wu, H., Ma, X.: A LLC resonant converter with a notch filter at secondary side for high step-up and wide voltage range applications. In: IEEE 2nd International Future Energy Electronics Conference (IFEEC), pp. 1–5. IEEE, Piscataway (2015)
17. Wu, X., Chen, H., Qian, Z.: 1-MHz LLC resonant DC transformer (DCX) with regulating capability. IEEE Trans. Ind. Electron. 63(5), 2904–2912 (2016)
18. Liao, Y., et al.: Single-stage DAB-LLC hybrid bidirectional converter with tight voltage regulation under DCX operation. IEEE Trans. Ind. Electron. 68(1), 293–303 (2021)
19. Guillod, T., Rothmund, D., Kolar J.,: Active magnetizing current splitting ZVS modulation of a 7 kV/400 V DC Transformer. IEEE Trans. Power Electron. 35(2), 1293–1305 (2020)
20. Fortes, G., Ladoux, P., Fabre, J., Flumian, D.: Characterization of a 300 kW isolated DC/DC converter using 3.3 kV SiC-MOSFETs. In: PCIM Europe Conference Proceedings. IEEE, Piscataway (2021)
21. Lo, Y., Lin, C., Hsieh, M., Lin, C.: Phase-shifted full-bridge series-resonant DC-DC converters for wide load variations. IEEE Trans. Ind. Electron. 58(6), 2572–2575 (2011)
22. Kim, J., Kim, C., Lee, J., Kim, Y., Youn, H., Moon, G.: A simple control scheme for improving light-load efficiency in a full-bridge LLC resonant converter. In: International Power Electronics Conference (IPEC-Hiroshima 2014 - ECCE ASIA), pp. 1743–1747. IEEE, Piscataway (2014)
23. Awasthi, A., Bagawade, S., Jain, P.: Analysis of a hybrid variable-frequency-duty-cycle-modulated low-Q LLC resonant converter for improving the light-load efficiency for a wide input voltage range. IEEE Trans. Power Electron. 36(7), 8476–8493 (2021)
24. Zheng, R., Liu, B., Duan, S.: Analysis and parameter optimization of start-up process for LLC resonant converter. IEEE Trans. Power Electron. 30(12), 7113–7122 (2015)
25. Besselmann, T., Mester, A., Dujic, D.: Power electronic traction transformer: efficiency improvements under light-load conditions. IEEE Trans. Power Electron. 29(8), 3971–3981 (2014)
26. Beiranvand, R., Rashidian, B., Zolghadri, M., Alavi, S.: Optimizing the normalized dead-time and maximum switching frequency of a wide-adjustable-range LLC resonant converter. IEEE Trans. Power Electron. 26(2), 462–472 (2011)

17554543, 2022, 14, Downloaded from https://ietresearch.onlinelibrary.wiley.com/doi/10.1049/pel2.12324 by Université De Toulouse 3, Wiley Online Library on [13/06/2023]. See the Terms and Conditions (https://onlinelibrary.wiley.com/terms-and-conditions) on Wiley Online Library for rules of use; OA articles are governed by the applicable Creative Commons License

27. Kim, C.: Optimal dead-time control scheme for extended ZVS range and burst-mode operation of phase-shift full-bridge (PSFB) converter at very light load. IEEE Trans. Power Electron. 34(11), 10823–10832 (2019)
28. Liu, J., Zhang, J., Zheng, T. Q., Yang, J.: A modified gain model and the corresponding design method for an LLC resonant converter. IEEE Trans. Power Electron. 32(9), 6716–6727 (2017)
29. Fabre, J., Ladoux, P., Caron, H., Verdicchio, A., Blaquière, J., Flumian, D., Sanchez, S.: Characterization and implementation of resonant isolated DC/DC converters for future MVdc railway electrification systems. IEEE Trans. Transp. Electrif. 7(2), 854–869 (2021)
30. Fabre, J., Blaquière, J., Verdicchio, A., Ladoux, P., Sanchez, S.: Characterization in ZVS mode of SiC MOSFET modules for MVDC applications. In: International Conference on Clean Electrical Power (ICCEP), pp. 470–477. IEEE, Piscataway (2019)
31. Lindenmüller, L., Alvarez, R., Bernet, S.: Optimization of a series resonant DCIDC converter for traction applications. In: IEEE Energy Conversion Congress and Exposition (ECCE), pp. 2201–2208. IEEE, Piscataway (2012)

How to cite this article: Fortes, G., Ladoux, P., Fabre, J., Flumian, D.: Analysis of light and no-load operation of a 300 kW resonant single active bridge based on 3.3 kV SiC-devices. IET Power Electron. 15, 1540–1549 (2022). https://doi.org/10.1049/pel2.12324

17554543, 2022, 14, Downloaded from https://ietresearch.onlinelibrary.wiley.com/doi/10.1049/pel2.12324 by Université De Toulouse 3, Wiley Online Library on [13/06/2023]. See the Terms and Conditions (https://onlinelibrary.wiley.com/terms-and-conditions) on Wiley Online Library for rules of use; OA articles are governed by the applicable Creative Commons License